

Linköping Studies in Science and Technology
Licentiate Thesis No. LIU-TEK-LIC 2006:5

Theoretical studies of microcavities and photonic crystals for lasing and waveguiding applications

Aliaksandr Rahachou



Linköpings universitet
INSTITUTE OF TECHNOLOGY

Department of Science and Technology
Linköping University, SE-601 74 Norrköping, Sweden
Norrköping, January 2006

**Theoretical studies of microcavities and photonic crystals for lasing
and waveguiding applications**

© 2006 Aliaksandr Rahachou

*Department of Science and Technology
Campus Norrköping, Linköping University
SE-601 74 Norrköping, Sweden*

ISBN 91-85457-99-X

ISSN 0280-7971

Printed in Sweden by UniTryck, Linköping, 2005

Abstract

This Licentiate presents the main results of theoretical study of light propagation in photonic structures, namely lasing disk microcavities and photonic crystals. In the first two papers (Paper I and Paper II) we present the developed novel scattering matrix technique dedicated to calculation of resonant states in 2D disk microcavities with the imperfect surface or/and inhomogeneous refractive index. The results demonstrate that the imperfect surface of a cavity has the strongest impact on the quality factor of lasing modes.

The generalization of the scattering-matrix technique to the quantum-mechanical case has been made in Paper III. That generalization has allowed us to treat a realistic potential of quantum-corrals (which can be considered as nanoscale analogues of optical cavities) and to obtain a good agreement with experimental observations.

Papers IV and V address the novel effective Green's function technique for studying propagation of light in photonic crystals. Using this technique we have analyzed characteristics of surface modes and proposed several novel surface-state-based devices for lasing/sensing, waveguiding and light feeding applications.

List of publications

- **Paper I:** A. Rahachou and I. Zozoulenko, *Effects of boundary roughness on a Q factor of whispering-gallery-mode lasing microdisk cavities*, J. Appl. Phys., vol. 94, pp. 7929-7931, 2003
- **Paper II:** A. Rahachou and I. Zozoulenko, *Scattering matrix approach to the resonant states and Q values of microdisk lasing cavities*, Appl. Opt., vol. 43, pp. 1761-1772, 2004
- **Paper III:** A. Rahachou and I. Zozoulenko, *Elastic scattering of surface electron waves in quantum corrals: Importance of the shape of the adatom potential*, Phys. Rev. B, vol. 70, pp. 233409 1-4, 2004
- **Paper IV:** A. Rahachou and I. Zozoulenko, *Light propagation in finite and infinite photonic crystals: The recursive Greens function technique*, Phys. Rev. B, vol. 72, pp. 155117 1-12, 2005
- **Paper V:** A. Rahachou and I. Zozoulenko, *Waveguiding properties of surface states in photonic crystals, physics/0510273, submitted to J. Light-wave Technol., 2005*

Acknowledgements

First of all I would like to thank Igor Zozoulenko for excellent supervision. He has spent really loads of time answering my stupid questions, discussing and pushing me to do something. :)

I am also grateful to Olle Inganäs for valuable discussions and initiation of this work.

Then, the other guys from our group - Martin Evaldsson and Siarhei Ihnatsenka. Despite we do a little bit different things, Martin and Siarhei not only always understand what I'm doing, but also can help with practical things like LaTeX, basic arithmetic or other important issues that bother me sometimes.

Of course, all people at ITN are very kind. Thank you, people! However, I'd like especially thank Aida Vitoria for good humor, which is, despite the weather, season or Dow-Jones average, remains sparkling!

Big thanks to my mother and father. Being far away from me, their love and support I feel every day.

Thanks to my girlfriend Olga Mishchenko. She supports and helps me from day to day, her love and kindness is just a miracle that I revealed here, in Sweden. Tack för det, Sverige! :)

I very appreciate the financial support from SI and ITN that enabled me to start my PhD here and to write this Licentiate.

Contents

Abstract	iii
List of publications	iv
Acknowledgements	v
Table of Contents	vi
1 INTRODUCTION	1
2 Photonic structures	5
2.1 Whispering-gallery-mode lasing microcavities	5
2.1.1 General principle of lasing operation	5
2.1.2 Total internal reflection and whispering-gallery modes	7
2.2 Surface states in photonic crystals	11
2.2.1 Photonic crystals	11
2.2.2 Surface states and their applications	15
3 Computational techniques	17
3.1 Available techniques for studying light propagation in photonic structures	17
3.2 Scattering matrix method	18
3.2.1 Application of the SM-method to quantum-mechanical problems	21
3.3 Green's function technique	22
4 Results	29
4.1 Effect of inhomogeneities on quality factors of disk microcavities (Papers I, II)	29
4.2 Quantum corrals (Paper III)	31
4.3 Surface-state lasers (Paper IV)	34
4.4 Surface-state waveguides (Paper V)	35

Bibliography

39

Chapter 1

INTRODUCTION

The idea of constructing chips that operate on light signals instead of electricity has engaged the minds of scientists during the last decade. Communicating photons instead of electrons would provide revolutionary breakthrough not only in the performance of devices, which can distribute data at the speed of light, but also in the capacity of transmitted data. By now, modern optical networks can provide such a bandwidth, that even the fastest state-of-the-art processors are unable to handle, and this trend seems to remain in nearest future. Furthermore, photons are not so strongly interacting as electrons/holes, which can significantly reduce power losses. Speaking about present time, only photonics provides solutions for high-dense modern data storage, like CDs and DVDs, whose capacity is constantly increasing.

Manufacturing practical photonic chips, however, brings in several challenges: first of all, lack of optical logic switches themselves as well as the principles of their operation, technological difficulties in manufacturing of novel photonic devices with the same well-developed processes for electronic chips, and, finally, the vital need of novel materials. In this regard, two the most promising "building blocks" of novel photonic chips have arized - *photonic crystals* and *lasing microcavities*, which, being intensively studied for the last decade, can provide the required microminiaturization and integration within photonic chips.

Along with unprecedented opportunities for integration of optical devices, photonic crystals exhibit a variety of unique physical phenomena. Photonic crystal is usually fabricated from the same semiconductor materials as electronic chips using common chipmaking techniques like photolithography. The main reason that has made photonic crystals so popular is their basic feature of having gaps in the energy spectrum that forbid light to travel at certain wavelengths. Such the gaps in the spectra provide very effective confinement of the light within photonic crystals that can be exploited as a basis for large number of photonic devices. Creating linear defects, for instance, will form low-loss waveguides, whereas point defects can act as high-quality microcavities. The another unique feature of photonic crystals with certain lattice parameters is negative refractive index that can be exploited for focusing and non-conventional distribution of light on a microscopic level. In additional real finite photonic crystals can support surface states on their boundaries, which can also be exploited for different purposes in photonic chips.

Optical microcavities are structures that confine of light and enable lasing action at microscopic scale. In conventional lasers, a significant portion of pump energy simply dissipates, and a rather high threshold power is required to initiate the lasing effect. In contrast, microcavities can be utilized to sustain highly efficient, almost "thresholdless", lasing action. Such the efficiency is related to the existence of the natural cavity resonances. These resonances are known as morphology-dependent resonances or *whispering gallery modes*. The origin of these resonances can be addressed to ray dynamics, when light

is trapped inside the cavity through the total internal reflection against its circumference. An ideal lossless cavity would trap this "rotating" light for infinitely long time and would have infinitely narrow lasing peaks. Combining microcavities into arrays or coupling them to waveguides creates variety of devices for sensing and filtering. Ultra high-quality microcavities can also be utilized in stunning applications like single atom detection.

The Thesis is organized as follows. In Chapter 2 we make a brief overview of photonic structures under the study, namely microdisk cavities and photonic crystals. Chapter 3 outlines the scattering matrix and Green's function techniques, and Chapter 4 summarizes the main results and contains necessary discussion.

Chapter 2

Photonic structures

2.1 Whispering-gallery-mode lasing microcavities

2.1.1 General principle of lasing operation

The word "LASER" is an acronym for *Light Amplification by Stimulated Emission of Radiation*. The output of a laser is a highly-coherent monochromatic (in a very ideal case) radiation, which can be pulsed or beamed in a visible, infrared or ultraviolet range. The power of a laser can vary from several milliwatts to megawatts.

The main, and the most crucial component of a laser is its active medium, which can be a solid, gas, liquid or semiconductor. In thermodynamic equilibrium nearly all atoms, ions or molecules (depending on the particular laser) of the active medium occupy their lowest energy level or "ground state". To produce laser action, the majority of atoms/ions/molecules should be "pumped" up into higher energy level, creating so called *population inversion*. Typical three-level structure is given in Fig. 2.1(a). Pump energy here excites atoms from the ground state to the short-lived level, which rapidly decays to the long-lived state. At random times, some of these excited atoms/ions/molecules will decay to the ground state on their own. Each decay is accompanied by emission of a single photon propagating in a random direction (*spontaneous emission*). However, if one of these photons encounters an excited atom/ion/molecule, it will drop down to a lower energy state and emit a new photon with exactly the same wavelength, phase, direction and polarization. This is called *stimulated emission*.

When a photon is emitted nearly parallel to the long side of the cavity (Fig. 2.1(b)) it will travel down to one of the mirrors and be able to get reflected back and forth many times. Along its way, it hits excited atoms/ions/molecules and

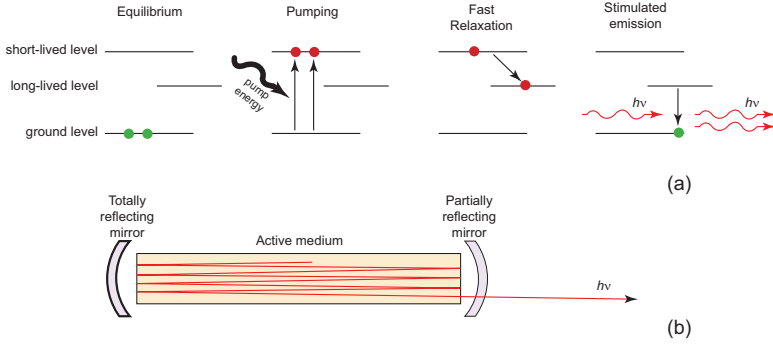


Figure 2.1: (a) Three-level diagram of a lasing system. (b) Lasing cavity.

"stimulates" them to emit up new photons. The process acts as an avalanche caused by a single photon which produces more and more photons via this stimulated emission process. When the energy of the photon beam becomes enough to make the beam escape a partially reflecting mirror, a highly monochromatic and coherent ray goes out. Depending of the type of a cavity the beam can be well collimated or appears to originate from a point/plane source.

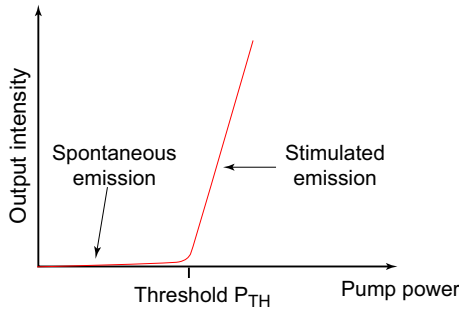


Figure 2.2: Threshold of a laser.

The one of the most important parameters of lasers is their *threshold* P_{TH} , that can be defined as the "critical" pumping power that corresponds the initiation of the stimulated emission (see Fig. 2.2). The threshold is proportional to the *threshold population difference*, i.e. the minimum positive difference in population between the long-lived and ground levels in Fig. 2.1:

$$N_T = N_{ll} - N_g \sim \frac{1}{c\tau_p} = \frac{\omega_0}{cQ} \quad (2.1)$$

where c is the speed of light, τ_p is a photon lifetime, ω_0 is the resonant frequency of a lasing mode and Q is the *quality factor* (Q -factor hereafter) of a lasing cavity. The main goal is, obviously, to minimize threshold, therefore maximize the photon lifetime and cavity quality factor. The Q -factor is strongly determined by the design of the cavity, several representative examples are given in Fig. 2.3.

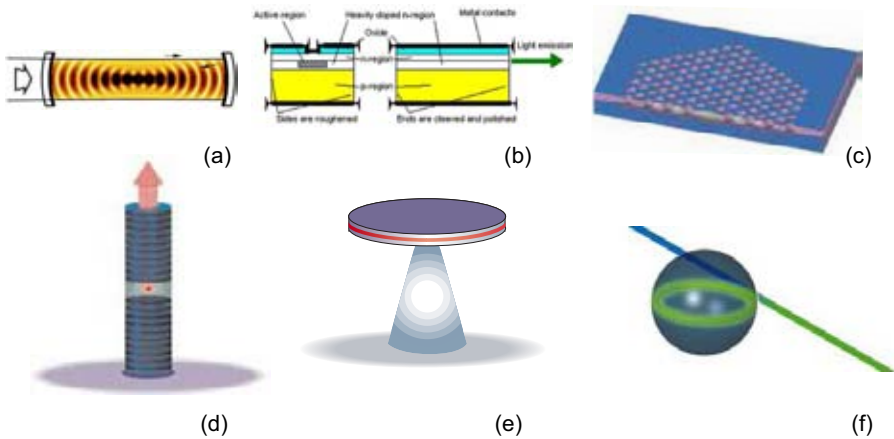


Figure 2.3: Different types of lasing cavities. (a) *Confocal resonator*. Employed in a variety of gas, solid-state and chemical lasers. Two confocal mirrors (one of them is partially reflecting) create a collimated beam parallel to the long side of the cavity. (b) *Laser diode*. The cavity is created by finely polished side walls of the structure. (c) *Photonic-crystal cavity*. The cavity is created by point inhomogeneity in a photonic-crystal lattice (see the next section for details). Q factor can reach 10^5 . (d) *Fabry-Perot resonator*. A set of stacked Bragg mirrors provides cavity confinement. Typical value of Q factor is ~ 2000 . (e) *Whispering-gallery disk microcavity*. The ray of light is trapped inside the cavity, undergoing multiple "bounces" against side wall due to the effect of total internal reflection. $Q \sim 10^4$. (f) *A spherical whispering-gallery droplet*. $Q \sim 10^8$. (c-f) are adopted from [1].

2.1.2 Total internal reflection and whispering-gallery modes

The one of the most well-known mechanisms of ray confinement in cavities is based on the effect of total internal reflection, which is presented in Fig. 2.4. The angle

$$\theta_c = \arcsin \frac{n_1}{n_2} \quad (2.2)$$

is called *the critical angle for total internal reflection*. At larger incidence angles θ_2 the ray remains fully reflected.

For curved boundaries (see Fig. 2.4 (b)) the regime of total internal reflection and the critical angle 2.2 have the same meaning. However, because of the diffraction at the curved boundary, a leakage takes place. Transmission coefficient for an electromagnetic wave penetrating a curved boundary in the regime of total internal reflection reads [2]

$$T = |T_F| \exp \left[-\frac{2}{3} \frac{nk\rho}{\sin^2(\theta)} (\cos^2 \theta_c - \cos^2 \theta)^{3/2} \right], \quad (2.3)$$

where T_F is the classical Fresnel transmission coefficient for an electromagnetic wave incident on a flat surface, k is a wavevector of the incident wave, ρ is the radius of curvature, and θ is the angle of incidence. The main goal, obviously, is to minimize T , in order to hold the light "trapped" inside the cavity as long as possible.

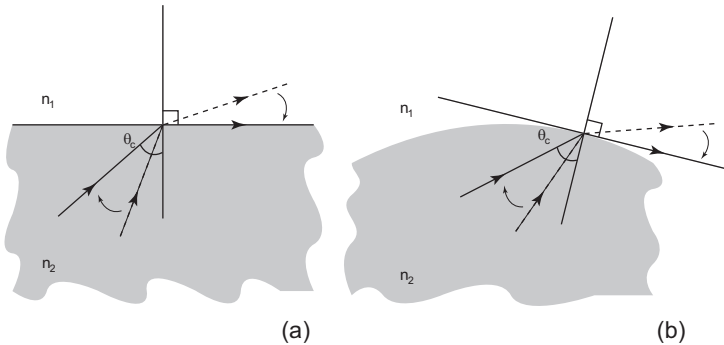


Figure 2.4: (a) Regime of the total internal reflection for (a) flat surface, (b) curved surface. The ray falls from medium 2 to boundary with medium 1 ($n_1 < n_2$) at incidence angle θ_2 and gets refracted to medium 1 at θ_1 . According to Snell's law, $n_1 \sin \theta_1 = n_2 \sin \theta_2$. If θ_2 is being increased, at some particular incidence angle θ_c , angle θ_1 becomes equal $\pi/2$ that corresponds full internal reflection of the incident ray.

The total internal reflection is the mechanism of light localization in *whispering-gallery cavities*. The term *whispering-gallery modes* (WGMs) came after the whispering gallery at St. Paul's Cathedral in London, see Fig. 2.5 (a), where quirk in its construction makes a whisper against its walls audible at the opposite side of the gallery. In whispering-gallery cavities (Fig. 2.5 (b)) WGMs occur at particular resonant wavelengths of light for a given cavity size. At these wavelengths the light undergoes total internal reflection at the cavity

surface and becomes confined within it for rather long time. In WGM regime

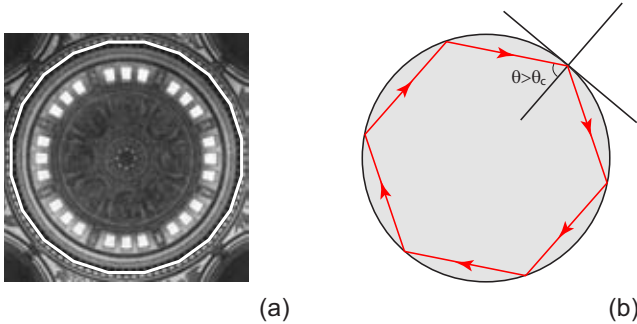


Figure 2.5: (a) The dome of the St. Paul's Cathedral in London. The white line outlines distribution of a WG-mode. (b) Multiple reflections of a whispering-gallery mode against the circumference of the cavity.

the light is localized near the circumference of the cavity and can be assigned a radial and angular mode number. The angular mode number n shows the number of wavelengths around the circumference of the cavity, and the radial mode number l – the number of maxima in the intensity of the electromagnetic field in the radial direction within the cavity (2.5(b)). The typical experimental spectrum of WG modes is given in Fig. 2.6(a).

Each whispering-gallery lasing mode of the cavity is characterized by its quality factor, which, by the definition of a Q -factor, is also related to the width of the resonant spectral line as

$$Q \equiv \frac{2\pi(\text{stored energy})}{(\text{energy loss per cycle})} = \frac{k}{\Delta k} \quad (2.4)$$

where Δk is the spectral line broadening taken at the half-amplitude of the lasing peak as it is shown in Fig. 2.6(b). Q -factor is also closely related to the time that the WG mode spends trapped within the cavity, so-called "Wigner delay time" [3]

$$Q = \omega \tau_D(\omega_{res}), \quad (2.5)$$

where ω is the resonant frequency.

The main reason of using whispering-gallery mode cavities is their high Q -values as well as excellent suitability for microminiaturization and integration within optical chips. Lasing whispering-gallery modes were first observed in spherical glass droplets. An important step was the development of microdisk semiconductor lasers, which exploited total internal reflection of light to achieve perfect mirror reflectivity. These lasers - the smallest in the world at the time -

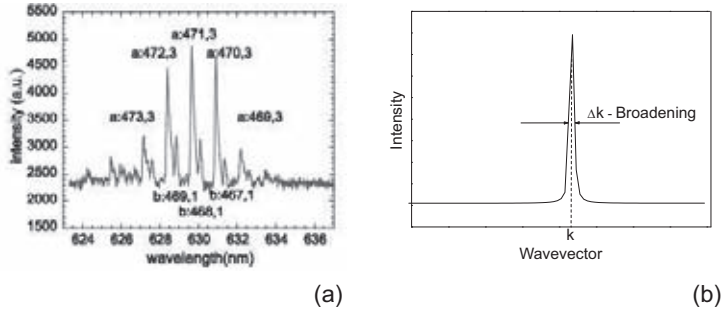


Figure 2.6: (a) Experimental spectrum of a whispering-gallery lasing microcavity [4]. Angular and radial mode numbers are also given. (b) Broadening of a lasing peak.

were invented and first demonstrated in 1991 by Sam McCall, Richard Slusher and colleagues at Bell Labs. Microdisk, -cylinder or -droplet lasers form a class of lasers based on circularly symmetric resonators, which lase in whispering-gallery modes. These tiny lasers, however, lack for directional emission due to their circular symmetry. The experimental microlasers of the Bell Labs and Yale team overcame this limitation. They were based on a new optical resonator shaped as a deformed cylinder (quadruple) and were highly directional. They exploited the concept of chaotic dynamics in asymmetric resonant cavities and were introduced by Nöckel and Stone at Yale in 1997.

At the present moment there have been reported cavities with Q -factors of order $\sim 10^8$ [5] with characteristic diameters $\sim 100\mu\text{m}$. The other advantages are their relatively easy fabrication process (i.e. they can be etched on a surface [4] or pedestal [6], highly-symmetrical spherical cavities [7] are formed through surface tension in silica); broad range of pumping methods (optical pump from the outside [4] or by the build-in quantum dots [6]; use of active polymers [8]); as well as the set of different shapes (disk, toroid, spherical, hexagonal, quadruple) possessing unique properties.

Unfortunately, quality factors in actual fabricated microcavities are normally several orders lower than the corresponding calculated values of ideal cavities. A degradation of the experimental Q -factors may be attributed to a variety of reasons including side wall geometrical imperfections, inhomogeneity of the diffraction index of the disk, effects of coupling to the substrate or pedestal and others. A detailed study of effects of the factors above on the characteristics and performance of the microcavity lasers appears to be of crucial importance for their optimization. Of the especial importance are the studies of surface roughness of the cavities, as it was demonstrated [9; 6; 10] to be the main factor affecting the Q -factor. Such the studies would require an

versatile method that can deal with complex geometry and variable refraction index in the cavity. In the next Chapter we develop a novel computational technique, which is capable to handle disk microcavities both with geometrical imperfections and refraction index inhomogeneities.

2.2 Surface states in photonic crystals

2.2.1 Photonic crystals

Photonic crystals (PCs) or *photonic bandgap materials* are artificial structures, which forbid propagation of light in particular ranges of frequencies, remaining transparent for others. Photonic band gaps were first predicted in 1987 by two physicists working independently. They were Eli Yablonovitch, at Bell Communications Research in New Jersey, and John Sajeev of the University of Toronto. An array of 1mm holes mechanically drilled in a slab of material with refractive index 3.6, latter to be known as Yablonovite, was found to prevent microwaves from propagating in any direction. Despite this remarkable success, it took more than a decade to fabricate photonic crystals that work in the near-infrared (780-3000 nm) and visible (450-750 nm) ranges of the spectrum and forbid light propagation in all directions. The main challenge was to find suitable materials and technologies to fabricate structures that are about a thousandth the size of the Yablonovite.

In order to understand light propagation in a photonic crystal let us compare that to the carrier transport in a semiconductor. The similarity between electromagnetic waves in PCs and de-Broglie electronic waves propagating in a crystalline solid has been utilized to develop theories of photonic crystals. This resemblance first arises in differential equations describing wave motion in both mediae. For electrons in semiconductor materials the Schrödinger equation reads as

$$\left(-\frac{\nabla^2}{2} + V(r)\right) \Psi(r) = E\Psi(r). \quad (2.6)$$

In a semiconductor crystal the atoms are arranged in a periodic lattice, and moving carriers experience a periodic atomic lattice potential

$$V(r+a) = V(r), \quad (2.7)$$

where a is a lattice constant. Then, there exists a wavevector k in the reciprocal lattice such that $\Psi(r)$ can be written as

$$\Psi(r) = e^{ikr} u_k(r), \quad (2.8)$$

where $u_k(r+a) = u_k(r)$ is a periodic function on the lattice. This expression is known as *Bloch's theorem*. Substituting that into Eq.2.6 one finds the

eigenfunctions $u_k(r)$ and eigenvalues E_k . The periodic potential causes formation of allowed energy bands separated by gaps. In perfect bulk semiconductor crystals no electrons or holes can be found in these energy gaps.

The situation also holds for photons travelling through periodic structures. Let us consider a periodic structure, e.g. a block of transparent dielectric material of high refractive index (related to a permittivity as $n = \sqrt{\epsilon}$) with "drilled" holes or, vice versa, a periodic set of high-index dielectric rods in air background. In this case the corresponding electromagnetic wave equation (*Maxwell's equation for magnetic field*) reads as:

$$\nabla \times \left(\frac{1}{\epsilon(\mathbf{r})} \nabla \times \right) \mathbf{H}(\mathbf{r}) = (\omega^2/c^2) \mathbf{H}(\mathbf{r}), \quad (2.9)$$

with the periodic dielectric function

$$\epsilon(\mathbf{r} + \mathbf{R}) = \epsilon(\mathbf{r}). \quad (2.10)$$

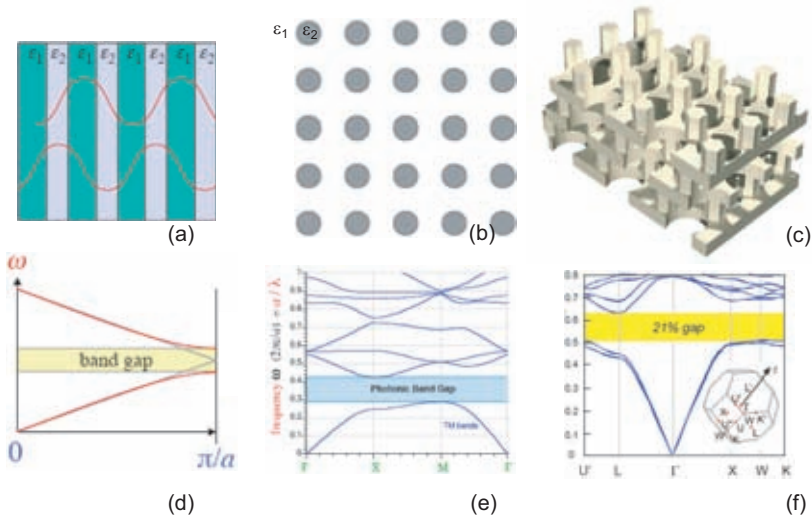


Figure 2.7: Examples (a-c) of 1D, 2D and 3D photonic crystals and (d-f) corresponding band structures. (adopted from [11])

For a photon, the periodic dielectric function acts just like the lattice potential that an electron or hole experiences propagating through a semiconductor crystal. If the contrast of refractive index is large, then most of the light will be confined either within the dielectric material or the air. This confinement causes formation intermingled allowed and forbidden energy regions. It

is possible to adjust the positions of bandgaps by changing the size of the air holes/rods in the material/air or by variation of the refractive index.

It is worth mentioning that the similarity between electrons in semiconductors and photons in photonic crystals is not complete. Unlike the Schrödinger's equation for electron waves, Maxwell's equation and electromagnetic waves are vectorial, which makes electromagnetic problems in general much more complicated.

The another important aspect is a periodicity of photonic crystals. If the periodicity in the refraction index holds only in one direction (i.e 1D photonic crystal), only light travelling perpendicularly to the periodically arranged layers is affected. Any 1D structure supports bandgaps. In 2D case, light propagating in the plane perpendicular to the rods will be affected. In order to make a complete bandgap for any direction of light propagation, a 3D structure have to be constructed. Fig. 2.7 illustrates 1D, 2D and 3D photonic crystals along with their band structures.

Photonic crystal devices normally operate in frequency regions corresponding bandgaps. The area of possible applications is constantly expanding, some representative examples are given in Fig. 2.8.

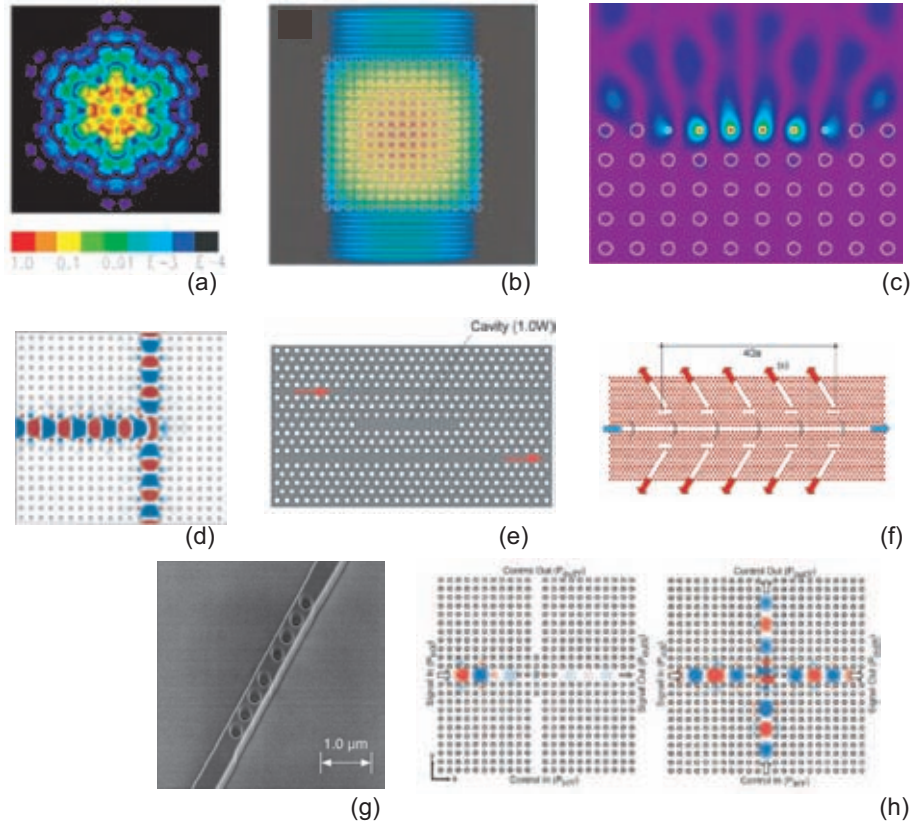


Figure 2.8: (a) *Low-threshold cavity lasers*. A properly designed point defect in photonic crystal can act as a lasing cavity. Strong confinement of the field within defect area enables one to achieve quality factors of order $\sim 10^6$ [12; 13]. (b) *Band-edge lasers*. Photonic crystal operates at the energy of the band edge, where velocity of light is very low, that causes long lifetime and Q -factor of the given state at this energy [14]. (c) *Surface-state lasers*. Breaking translation symmetry of the surface of a photonic crystal turns a surface mode into a resonant state with high Q -factor. The unique feature of such a cavity is its location on the surface of a PC [15; 16]. (d) *Low-loss waveguides with wide curvature*. In optical integrated circuits, the construction of low-loss waveguides with wide curvature is essential. When PCs are fabricated using low-loss dielectric materials, they act as perfect mirrors for frequencies in the gap [17]. (e,f) *Channel add/drop filters*. Enable switching and redistributing light of certain frequencies between two or more waveguides [13; 18]. (g) *Photonic bandgap microcavity in a dielectric waveguide*. Acts as a filter in dielectric waveguides, suppresses all frequency range except for frequencies of the resonant states of a PC-cavity [19]. (h) *Optical transistor*. Based on Kerr effect. The light intensity of the control beam (transverse waveguide) affects the Kerr cell, switching the light in the longitudinal waveguide [20].

2.2.2 Surface states and their applications

Surface states or *surface modes* is a special type of states in a photonic crystal that reside at the interface between a semi-infinite PC and open space, decaying both into the crystal and air [21]. Not every boundary of a photonic crystal supports surface states. For example, surface modes can be always found on the surface of a truncated 2D hexagonal array of holes in a material. At the same time, no surface state can be found on the unmodified surface of a semi-infinite square array of cylinders in the air background. In this case surface states appear in a bandgap of a square-lattice photonic crystal when its boundary is modified by, e.g., truncating the surface rods, shrinking or increasing their size, or creating more complex surface geometry [21; 22; 23; 24]. The examples of structures supporting surface states along with their band diagrams are given in Fig. 2.9.

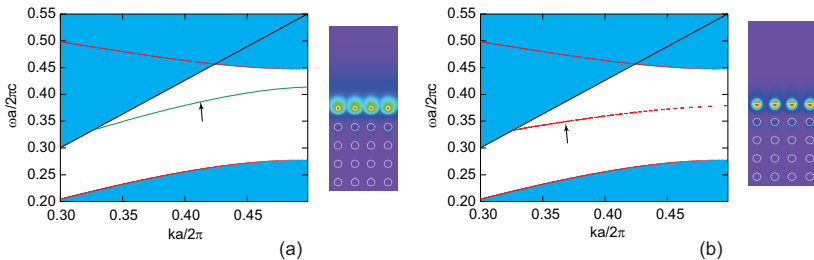


Figure 2.9: Band structures for TM modes in ΓX direction of square-lattice photonic crystals composed of rods with diameter $D = 0.4a$ (a is the lattice constant) and permittivity $\varepsilon = 8.9$ along with the projected surface modes. The surface rods are (a) reduced to $d = 0.2a$ and (b) half-truncated. Right panels show the intensity of E_z component of surface-mode dispersion curves at energies denoted with arrows.

So, why do the surface states in PCs attract our attention? Thanks to their unique location, on the surface of a photonic crystal, they open up new possibilities of coupling photonic devices to external light sources, stimulate directional beaming [25] from the waveguide opening on the surface. It is worth to emphasize that the surface mode residing on the infinitely long boundary of a semi-infinite crystal represents a truly bound Bloch state with the infinite lifetime and Q -factor, and consequently does not couple or leak to air states. We have recently shown (see Paper V) that this feature enables surface states to be exploited as high-quality surface waveguides and directional beamers, which, being allocated on the surface of a PC, bring in unique opportunities in redistributing light in photonic chips. It has been also demonstrated (Paper IV), [15; 16] that when the translational symmetry along the boundary of the

semi-infinite crystal is broken, the Bloch surface mode turns into a resonant state with a finite lifetime. This effect can be utilized for lasing and sensing applications.

Chapter 3

Computational techniques

3.1 Available techniques for studying light propagation in photonic structures

By far, the most popular method for the theoretical description of light propagation photonic systems is the finite-difference time-domain method (FDTD) introduced by Yee [26]. The method is proven to be rather flexible and has been successfully applied to study of microcavities and photonic crystal structures. However, despite its speed and flexibility, the FDTD technique has a serious limitation related to the finiteness of the computational domain. As the result, an injected pulse experiences spurious reflections from the domain boundaries that leads to mixing between the incoming and reflected waves. In order to overcome this bottleneck the so-called perfectly matched layer condition has been introduced [27]. However, even using this technique, a sizable portion of the incoming flux can still be reflected back [28]. In many cases the separation of spurious reflected pulses is essential for the interpretation of the results, and this separation can only be achieved by increase of the size of a computational domain. This may enormously increase the computational burden, as the stability of the FDTD algorithm requires a sufficiently small time step. A severe disadvantage of this technique in application to microcavities with tiny surface imperfections is that the smooth geometry of the cavity has to be mapped into a discrete grid with very small lattice constant. This makes the application of this method to the problems, when the small imperfection are studied, rather impractical in terms of both computational power and memory.

For studying microcavities, the number of boundary-element methods was applied. Their essence is that they reduce the Helmholtz equation in the infinite two-dimensional space into contour integral equations defined at the cavity boundaries. These methods include the T -matrix technique [29; 30], the bound-

ary integral methods [31; 32] and others [33]. In general, they are computationally effective and capable to deal with the cavities of arbitrary geometry. However, they require the refraction index be constant within the cavity.

Numerous theoretical approaches have been developed to calculate the photonic band structure for 2D and 3D photonic crystals. Plane-wave method [34; 35; 36], for instance, allows one to calculate band structures of PCs having known their Brillouin zones. Unfortunately, despite its ease to implement and stability, the method is not suitable for dispersive materials (that was actually resolved in [37]). Moreover, for complex structures (involving e.g. waveguides, cavities or surfaces) a large supercell has to be chosen that strongly increases the number of plane waves in the expansion and makes the method extremely computationally consuming.

The problem of the spurious reflections from the computational domain boundaries does not arise in the methods based on the transfer-matrix technique [38] where the transfer matrix relates incoming and outgoing fields from one side of the structure to those at another side. However, such the mixing leads to divergence of the method. The scattering-matrix (SM) techniques [39; 40; 41; 42], in contrast, are free of this drawback, as the scattering matrix relates incident and outgoing fields and their mixing is avoided. The other approaches, free of spurious reflections, are e.g. a multiple multipole method [43] and a dyadic Green's function method [44] based on the analytical expression for the Green's function for an empty space. However, the latter cannot be applied to sufficiently large structures due to gigantic memory requirements.

3.2 Scattering matrix method

In this Section we present a method dedicated for calculation of resonant states in dielectric disk microcavities. We developed this technique being motivated by the fact that *there are no theoretical tools so far, which are able to study microcavities both with tiny surface roughness and refractive index inhomogeneities*. The method is capable to handle cavities with boundary roughness as well as inhomogeneous refractive index within the cavity. Because the majority of experiments are performed only with the lowest transverse mode occupied, the transverse (z -) dependence of the field is neglected and computations are performed in 2D. The two-dimensional Helmholtz equation for z -components of electromagnetic field reads as

$$\left(\frac{\partial^2}{\partial r^2} + \frac{1}{r} \frac{\partial}{\partial r} + \frac{1}{r^2} \frac{\partial^2}{\partial \varphi^2} \right) \Psi(r, \varphi) + (kn)^2 \Psi(r, \varphi) = 0, \quad (3.1)$$

where $\Psi = E_z$ (H_z) for TM (TE)-modes, n is the refractive index and k is the wave vector in vacuum. Remaining components of the electromagnetic field can be derived from E_z (H_z) in a standard way.

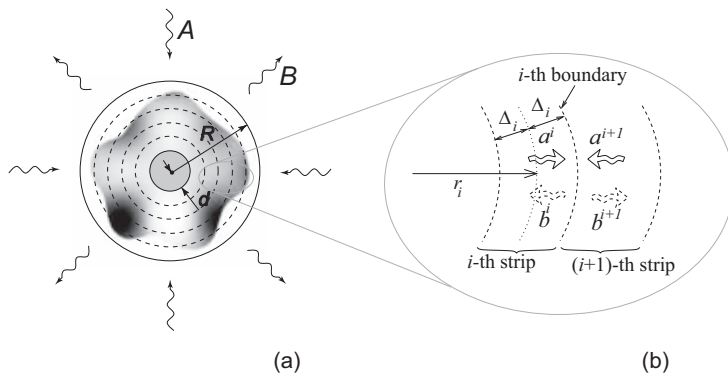


Figure 3.1: (a) Sketch of the geometry of a cavity with the refractive index n surrounded by air. The domain is divided in three regions. In the inner ($r < d$) and in the outer regions ($r > R$) the refractive indexes are constant. In the intermediate region $d < r < R$ the refractive index n is a function of both r and φ . (b) The intermediate region is divided by N concentric rings of the width 2Δ ; ρ_i is the distance to the middle of the i -th ring. Within each ring the refractive coefficient is regarded as a function of the angle only and a constant in r . States a^i, a^{i+1} propagate (or decay) towards the i -th boundary, whereas states b^i, b^{i+1} propagate (or decay) away of this boundary. The i -th boundary is defined as the boundary between the i -th and $(i + 1)$ -th rings.

Then the system is divided in three regions, the outer region, ($r > R$), the inner region, ($r < d$), and the intermediate region, ($d < r < R$), see Fig. 3.1(a). We choose R and d in such a way that in the outer and the inner regions the refractive indexes are constant whereas in the intermediate region n is a function of both r and φ . In these regions the solutions to the Helmholtz equation are analytical and can be written in the forms

$$\Psi_{in} = \sum_{q=-\infty}^{+\infty} a_q^0 J_q(nkr) e^{iq\varphi}, \quad (3.2)$$

for the inner region, where J_q is the Bessel function of the first kind, and

$$\Psi_{out} = \sum_{q=-\infty}^{+\infty} \left(A_q H_q^{(2)}(kr) + B_q H_q^{(1)}(kr) \right) e^{iq\varphi}, \quad (3.3)$$

for the outer region, where $H_q^{(1)}, H_q^{(2)}$ are the Hankel functions of the first and second kind of the order q describing respectively incoming and outgoing waves

respectively.

Then, the scattering matrix \mathbf{S} is defined in a standard formulation [45; 46]

$$B = \mathbf{S}A, \quad (3.4)$$

where A, B are the column vectors composed of the expansion coefficients A_q, B_q in Eq. (3.3). The matrix element $S_{q'q} = (\mathbf{S})_{q'q}$ gives a probability amplitude of the scattering from the incoming state q into the outgoing state q' .

The intermediate region is divided into narrow concentric rings where the refraction index depends only on the angle φ (outlined in Fig. 3.1(b)). The solutions to the Helmholtz equation in these rings can be expressed as superpositions of cylindrical waves. At each i -th boundary between the strips we define a local scattering matrix, which connects states propagating (or decaying) towards the boundary with those propagating (or decaying) outwards the boundary as

$$\begin{pmatrix} b^i \\ b^{i+1} \end{pmatrix} = \mathbf{S}^i \begin{pmatrix} a^i \\ a^{i+1} \end{pmatrix}. \quad (3.5)$$

Local scattering matrices \mathbf{S}^i are derived using the requirement of the continuity of the tangential components for the E_z - and H_z -fields at the i -th boundary. The essence of the scattering matrix technique is the successive combination of the scattering matrices in the neighboring regions. Thus, combining the scattering matrices for the i -th and $(i+1)$ -th boundaries, \mathbf{S}^i and \mathbf{S}^{i+1} , one obtains the aggregate scattering matrix $\tilde{\mathbf{S}}^{i,i+1} = \mathbf{S}^i \otimes \mathbf{S}^{i+1}$ that relates the outgoing and incoming states in the rings i and $i+2$ [45; 46]

$$\begin{aligned} \begin{pmatrix} b^i \\ b^{i+2} \end{pmatrix} &= \tilde{\mathbf{S}}^{i,i+1} \begin{pmatrix} a^i \\ a^{i+2} \end{pmatrix}, \\ \tilde{\mathbf{S}}_{11}^{i,i+1} &= \mathbf{S}_{11}^i + \mathbf{S}_{12}^i \mathbf{S}_{11}^{i+1} (\mathbf{I} - \mathbf{S}_{22}^i \mathbf{S}_{11}^{i+1})^{-1} \mathbf{S}_{21}^i, \\ \tilde{\mathbf{S}}_{12}^{i,i+1} &= \mathbf{S}_{12}^i (\mathbf{I} - \mathbf{S}_{11}^{i+1} \mathbf{S}_{22}^i)^{-1} \mathbf{S}_{12}^{i+1}, \\ \tilde{\mathbf{S}}_{21}^{i,i+1} &= \mathbf{S}_{21}^{i+1} (\mathbf{I} - \mathbf{S}_{22}^i \mathbf{S}_{11}^{i+1})^{-1} \mathbf{S}_{21}^i, \\ \tilde{\mathbf{S}}_{22}^{i,i+1} &= \mathbf{S}_{22}^{i+1} + \mathbf{S}_{21}^{i+1} (\mathbf{I} - \mathbf{S}_{22}^i \mathbf{S}_{11}^{i+1})^{-1} \mathbf{S}_{22}^i \mathbf{S}_{12}^{i+1}, \end{aligned} \quad (3.6)$$

where the matrices $\mathbf{S}_{11}, \mathbf{S}_{12}, \dots$ define the respective matrix elements of the block matrix \mathbf{S} . Combining all the local matrices $0 \leq i \leq N$ in this manner one finally obtains the total matrix $\tilde{\mathbf{S}}^{0,N} = \mathbf{S}^0 \otimes \mathbf{S}^1 \otimes \dots \otimes \mathbf{S}^N$ relating the scattering states in the outer region ($i = N$) and the states in the inner region ($i = 0$), which after straightforward algebra is transformed to matrix \mathbf{S} Eq. (3.4).

The scattering matrix provides the complete information about the system under study. In order to identify resonances, one introduces Wigner time-delay

matrix [3] averaged over incoming states as

$$\tau_D(k) = \frac{1}{icM} \frac{d}{dk} \ln[\det(\mathbf{S})], \quad (3.7)$$

where M is a number of incoming states. It is interesting to note that Smith in his original paper, dealing with quantum mechanical scattering [3], chose a letter "Q" to define the lifetime matrix of a quantum system because of a close analogy to the definition of the Q -factor of a cavity in electromagnetic theory. The resonant states of the cavity are manifested as peaks in the delay time whose positions determine the resonant frequencies ω_{res} , and the heights are related to the Q -value of the cavity according to (2.5).

3.2.1 Application of the SM-method to quantum-mechanical problems

The developed scattering-matrix method was generalized to quantum-mechanical problems. This is possible thanks to the direct similarity between the Helmholtz and Schrödinger equations [46]:

Photons	→	Electrons
$\nabla^2 E = -\omega^2 \varepsilon E$	→	$\nabla^2 \Psi = -2m/\hbar^2 [E - U] \Psi$
E	→	Ψ
Polarization	→	Spin
$S \sim \Re[-iE^* \times (\nabla \times E)]$	→	$J \sim \Re[-i\Psi^* \nabla \Psi]$
$\exp(-i\omega t)$	→	$\exp(-iEt/\hbar)$

The method solves a problem of quantum-mechanical (QM) scattering in *quantum corral* [47; 48] structures, which can be considered as QM analogues of disk microcavities. We calculate scattering wave function, from which one can extract spectra and the differential conductance dI/dV of the STM tunnel junction (which is proportional to the local density of states (LDOS))

$$dI/dV \sim \text{LDOS}(\mathbf{r}, E) = \sum_q |\psi_q(\mathbf{r})|^2 \delta(E - E_q), \quad (3.8)$$

where $\psi_q(\mathbf{r})$ are the scattering eigenstates of the Hamiltonian \hat{H} . The advance of the method is its ability to treat a realistic smooth potential within the corral structure.

3.3 Green's function technique

In order to study light propagation in 2D photonic-crystal structures, we have developed a novel *recursive Green's function technique*. In contrast with FDTD methods, the presented Green's function technique is free of the effect of spurious reflections. The Green's function of the photonic structure is calculated recursively by adding slice by slice on the basis of Dyson's equation, that relaxes memory requirements and makes the method easy-parallelizable. In order to account for the infinite extension of the structure both into the air and into the space occupied by the photonic crystal we make use of the so-called "surface Green's functions" that propagate the electromagnetic fields into (and from) infinity. The method is widely used in quantum-mechanical calculations [49] and has been proven to be unconditionally stable.

We start from Helmholtz equation, which for 2D case (permittivity $\varepsilon(r)$ is constant in z direction) decouples in two sets of equations for the TE modes

$$\frac{\partial}{\partial x} \frac{1}{\varepsilon_r} \frac{\partial}{\partial x} H_z + \frac{\partial}{\partial y} \frac{1}{\varepsilon_r} \frac{\partial}{\partial y} H_z + \frac{\omega^2}{c^2} H_z = 0 \quad (3.9)$$

and for the TM modes

$$\frac{1}{\varepsilon_r} \left(\frac{\partial^2 E_z}{\partial x^2} + \frac{\partial^2 E_z}{\partial y^2} \right) + \frac{\omega^2}{c^2} E_z = 0. \quad (3.10)$$

Let us now rewrite the equations (3.9), (3.10) in an operator form [50]

$$\mathbf{L}f = \left(\frac{\omega}{c} \right)^2 f \quad (3.11)$$

where the *Hermitian* differential operator \mathbf{L} and the function f read

$$\text{TE modes: } f \equiv H_z; \quad \mathbf{L}_{TE} = -\frac{\partial}{\partial x} \frac{1}{\varepsilon_r} \frac{\partial}{\partial x} - \frac{\partial}{\partial y} \frac{1}{\varepsilon_r} \frac{\partial}{\partial y}, \quad (3.12)$$

$$\text{TM modes: } f = \sqrt{\varepsilon_r} E_z; \quad \mathbf{L}_{TM} = -\frac{1}{\sqrt{\varepsilon_r}} \left(\frac{\partial^2}{\partial x^2} + \frac{\partial^2}{\partial y^2} \right) \frac{1}{\sqrt{\varepsilon_r}}. \quad (3.13)$$

For the numerical solution, Eqs. (3.11)-(3.13) have to be discretized, $x, y \rightarrow m\Delta, n\Delta$, where Δ is the grid step. Using the following discretization of the differential operators in Eqs. (3.12),(3.13),

$$\begin{aligned} \Delta^2 \frac{\partial}{\partial x} \xi(x) \frac{\partial f(x)}{\partial x} &\rightarrow \xi_{m+\frac{1}{2}} (f_{m+1} - f_m) - \xi_{m-\frac{1}{2}} (f_m - f_{m-1}), \\ \Delta^2 \frac{\partial^2}{\partial x^2} \xi(x) f(x) &\rightarrow \xi_{m+1} f_{m+1} - 2\xi_m f_m + \xi_{m-1} f_{m-1} \end{aligned} \quad (3.14)$$

one arrives to the finite difference equation

$$\begin{aligned} v_{m,n} f_{m,n} - u_{m,m+1;n,n} f_{m+1,n} - u_{m,m-1;n,n} f_{m-1,n} - \\ - u_{m,m;n,n+1} f_{m,n+1} - u_{m,m;n,n-1} f_{m,n-1} = \left(\frac{\omega \Delta}{c} \right)^2 f_{m,n}, \end{aligned} \quad (3.15)$$

where the coefficients v, u are defined for the cases of TE and TM modes as follows

$$\text{TE modes: } f_{m,n} = H_{z m,n}; \quad \xi_{m,n} = \frac{1}{\varepsilon_{r m,n}}, \quad (3.16)$$

$$\begin{aligned} v_{m,n} &= \xi_{m+\frac{1}{2},n} + \xi_{m-\frac{1}{2},n} + \xi_{m,n+\frac{1}{2}} + \xi_{m,n-\frac{1}{2}}, \\ u_{m,m+1;n,n} &= \xi_{m+\frac{1}{2},n}, \quad u_{m,m-1;n,n} = \xi_{m-\frac{1}{2},n}, \\ u_{m,m;n,n+1} &= \xi_{m,n+\frac{1}{2}}, \quad u_{m,m;n,n-1} = \xi_{m,n-\frac{1}{2}}; \end{aligned}$$

$$\text{TM modes: } f_{m,n} = \sqrt{\varepsilon_{r m,n}} E_{z m,n}; \quad \xi_{m,n} = \frac{1}{\sqrt{\varepsilon_{r m,n}}} \quad (3.17)$$

$$\begin{aligned} v_{m,n} &= 4\xi_{m,n}^2, \\ u_{m,m+1;n,n} &= \xi_{m,n} \xi_{m+1,n}, \quad u_{m,m-1;n,n} = \xi_{m-1,n} \xi_{m,n}, \\ u_{m,m;n,n+1} &= \xi_{m,n+1} \xi_{m,n}, \quad u_{m,m;n,n-1} = \xi_{m,n} \xi_{m,n-1}. \end{aligned}$$

A convenient and common way to describe finite-difference equations on a discrete lattice is to introduce the corresponding *tight-binding* operator. For this purpose one first introduces creation and annihilation operators, $a_{m,n}^+$, $a_{m,n}$. Let the state $|0\rangle \equiv |0, \dots, 0_{m,n}, \dots, 0\rangle$ describe an empty lattice, and the state $|0, \dots, 0, 1_{m,n}, 0, \dots, 0\rangle$ describe an excitation at the site m, n . The operators $a_{m,n}^+$, $a_{m,n}$ act on these states according to the rules [49]

$$\begin{aligned} a_{m,n}^+ |0\rangle &= |0, \dots, 0, 1_{m,n}, 0, \dots, 0\rangle, \\ a_{m,n}^+ |0, \dots, 0, 1_{m,n}, 0, \dots, 0\rangle &= 0, \end{aligned} \quad (3.18)$$

and

$$\begin{aligned} a_{m,n} |0\rangle &= 0, \\ a_{m,n} |0, \dots, 0, 1_{m,n}, 0, \dots, 0\rangle &= |0\rangle, \end{aligned} \quad (3.19)$$

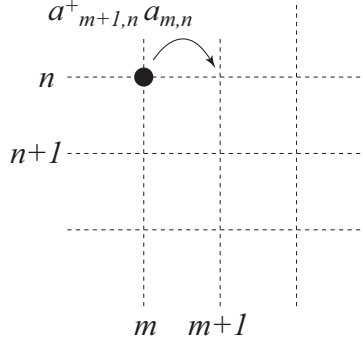


Figure 3.2: Forward hopping term in Eq. 3.22.

and they obey the following commutational relations

$$\begin{aligned} [a_{m,n}, a_{m,n}^+] &= a_{m,n} a_{m,n}^+ - a_{m,n}^+ a_{m,n} = \delta_{m,n}, \\ [a_{m,n}, a_{m,n}] &= [a_{m,n}^+, a_{m,n}^+] = 0. \end{aligned} \quad (3.20)$$

Consider an operator equation

$$\hat{\mathcal{L}}|f\rangle = \left(\frac{\omega\Delta}{c}\right)^2 |f\rangle, \quad (3.21)$$

where the Hermitian operator

$$\begin{aligned} \hat{\mathcal{L}} = \sum_{m,n} & (v_{m,n} a_{m,n}^+ a_{m,n} - \\ & - u_{m,m+1;n,n} a_{m,n}^+ a_{m+1,n} - u_{m+1,m;n,n} a_{m+1,n}^+ a_{m,n} - \\ & - u_{m,m;n,n+1} a_{m,n}^+ a_{m,n+1} - u_{m,m;n+1,n} a_{m,n+1}^+ a_{m,n}) \end{aligned} \quad (3.22)$$

acts on the state

$$|f\rangle = \sum_{m,n} f_{m,n} a_{m,n}^+ |0\rangle. \quad (3.23)$$

It is important to stress that terms 2 and 3 in Eq. (3.22) describe forward and backward hopping between two neighboring sites of the discretized domain in x -direction, and terms 4 and 5 denote similar hopping in y -direction. Figure 3.2 illustrates the first term in (3.22), the forward hopping from m -th to $m+1$ -th site. Substituting the above expressions for $\hat{\mathcal{L}}$ and $|f\rangle$ in Eq. (3.21) and using the commutation relations and the rules Eqs. (3.18)-(3.20), it is straightforward

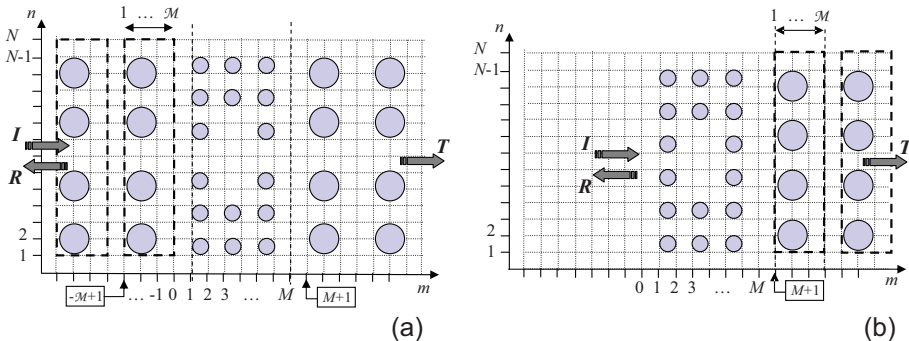


Figure 3.3: Schematic illustration of the system under study defined in a supercell of the width N . The internal region of the structure occupies M slices. Two representative cases are shown: (a) external regions are semi-periodic photonic crystals with the period M , (b) external regions represent a semi-infinite periodic photonic crystal with the period M to the right and air to the left. Arrows indicate the directions on the incoming (I), reflected (R) and transmitted (T) waves.

to demonstrate that the operator equation (3.21) is equivalent to the finite difference equation (3.15).

Let us now specify structures under study. We consider light propagation through a photonic structure defined in a supercell of the width N , where one assumes the cyclic boundary condition (i.e. the row $n = N + 1$ coincides with the row $n = 1$). The photonic structure occupies a finite internal region consisting of M slices ($1 \leq m \leq M$).

The external regions are semi-infinite supercells extending into regions $m \leq 0$ and $m \geq M + 1$. The supercells can represent air (or a material with a constant refractive index) or a periodic photonic crystal. Figure 3.3 shows two representative examples where (a) the semi-infinite waveguides represent a *periodic* photonic crystal with the period M , and (b) a photonic structure is defined at the boundary between air and the semi-infinite photonic crystal.

We define Green's function of the operator $\hat{\mathcal{L}}$ in a standard way

$$\left((\omega\Delta/c)^2 - \hat{\mathcal{L}} \right) G(\omega) = \hat{\mathbb{1}}, \quad (3.24)$$

where $\hat{\mathbb{1}}$ is the unitary operator. The knowledge of the Green's function allows one to calculate the transmission and reflection coefficients. Indeed, let us write down the solution of Eq. (3.21) as a sum of two terms, the incoming state $|\psi^i\rangle$ and the system response $|\psi\rangle$ representing whether the transmitted $|\psi^t\rangle$ or reflected $|\psi^r\rangle$ states, $|f\rangle = |\psi^i\rangle + |\psi\rangle$. Substituting $|f\rangle$ into Eq. (3.21)

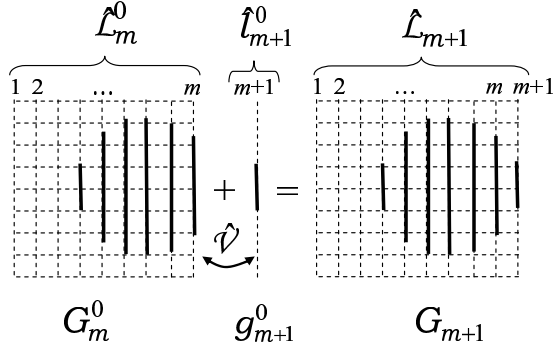


Figure 3.4: Schematic illustration of the application of Dyson's equation for calculation of Green's function for a composed structure consisting of $m+1$ slices.

and using the formal definition of the Green's function Eq. (3.24), the solution of Eq. (3.21) can be written in the form

$$|\psi\rangle = G \left(\widehat{\mathcal{L}} - (\omega\Delta/c)^2 \right) |\psi^i\rangle. \quad (3.25)$$

Calculation of the whole structure starts from the internal region (i.e for the slices $1 \leq m \leq M$ in Fig. 3.3). The recursive technique based on Dyson's equation is utilized, see Fig. 3.4. Our goal is to calculate Green's function of the composed structure, G_{m+1} , consisting of $m + 1$ slices. The operator corresponding to this structure can be written down in the form

$$\widehat{\mathcal{L}}_{m+1} = \widehat{\mathcal{L}}_m^0 + \widehat{l}_{m+1}^0 + \widehat{\mathcal{V}}, \quad (3.26)$$

where the operators $\widehat{\mathcal{L}}_m^0$ and \widehat{l}_{m+1}^0 describe respectively the structure composed of m slices and the stand-alone $(m + 1)$ -th slice, and $\widehat{\mathcal{V}} = \widehat{\mathcal{V}}_{m,m+1} + \widehat{\mathcal{V}}_{m+1,m}$ is the perturbation operator describing the hopping between the m -th and $(m + 1)$ -th slices,

$$\widehat{\mathcal{V}} = \widehat{\mathcal{V}}_{m+1,m} + \widehat{\mathcal{V}}_{m,m+1}. \quad (3.27)$$

The Green's function of the composed structure, G_{m+1} , can be calculated on the basis of Dyson's equation:

$$\begin{aligned} G_{m+1} &= G^0 + G^0 \widehat{\mathcal{V}} G_{m+1}, \\ G_{m+1} &= G^0 + G_{m+1} \widehat{\mathcal{V}} G^0, \end{aligned} \quad (3.28)$$

where G^0 is the ‘unperturbed’ Green’s function corresponding to the operators $\widehat{\mathcal{L}}_m^0$ or \widehat{l}_{m+1}^0 . Thus, starting from Green’s function for the first slice g_1^0 and adding recursively slice by slice we are in the position to calculate Green’s function of the internal structure consisting of M slices. Explicit expressions following from Eqs. (3.28) and used for the recursive calculations read as

$$\begin{aligned} G_{m+1}^{m+1,m+1} &= (I - g_{m+1}^0 U_{m+1,m} (G_m^0)^{m,m} U_{m,m+1})^{-1} g_{m+1}^0, \\ G_{m+1}^{m+1,1} &= G_{m+1}^{m+1,m+1} U_{m+1,m} (G_m^0)^{m,1}, \\ G_{m+1}^{1,1} &= (G_m^0)^{1,1} + (G_m^0)^{1,m} U_{m,m+1} G_{m+1}^{m+1,1}, \\ G_{m+1}^{1,m+1} &= (G_m^0)^{1,m} U_{m,m+1} G_{m+1}^{m+1,m+1}, \end{aligned} \quad (3.29)$$

where the upper indexes define the matrix elements of the Green’s function.

The next step is attaching left and right semi-infinite leads to the internal region. Starting with the left waveguide, one writes

$$\widehat{\mathcal{L}}_{int+left} = \widehat{\mathcal{L}}_{int} + \widehat{\mathcal{L}}_{left} + \widehat{\mathcal{V}}, \quad (3.30)$$

where the operators $\widehat{\mathcal{L}}_{int+left}$, $\widehat{\mathcal{L}}_{int}$ and $\widehat{\mathcal{L}}_{left}$ describe respectively the system representing the internal structure + the left waveguide, the internal structure, and the left waveguide. The perturbation operator $\widehat{\mathcal{V}}$ describes the hopping between the left waveguide and the internal structure. Applying then the Dyson’s equation in a similar way as it has been described above,

$$G_{int+left} = G^0 + G^0 \widehat{\mathcal{V}} G_{int+left}, \quad (3.31)$$

we are in the position to find the Green’s function $G_{int+left}$ of the system representing the internal structure + the left waveguide. G^0 in Eq. (3.31) is an ‘unperturbed’ Green’s function corresponding to the internal structure and the semi-infinite waveguide (the ”surface Green’s function” Γ). The physical meaning of the surface Green’s function Γ is that it propagates the electromagnetic fields from the boundary slice of the semi-infinite waveguide (supercell) into infinity. A method for calculation of the surface Green’s functions both for the case of a semi-infinite homogeneous dielectrics, as well as for the case of a semi-infinite photonic crystal in a waveguide geometry is given in Paper IV. Having calculated the Green’s function $G_{int+left}$ on the basis of Eq. (3.31), one proceeds in a similar way by adding the right waveguide and calculating with the help of the Dyson’s equation the total Green’s function G of the whole system.

Having calculated matrix elements for the complete system, $G^{M+1,0}$, $G^{0,M+1}$, $G^{0,0}$, $G^{M+1,M+1}$, one can easily relate them to the transmission T and reflec-

tion R coefficients of the system (see Paper IV for details)

$$\Phi_{M+1}T = -G^{M+1,0}(U_{0,1}\Phi_{-\mathcal{M}+1}K_l - \Gamma_l^{-1}\Phi_0), \quad (3.32)$$

$$\Phi_0R = -G^{0,0}(U_{0,1}\Phi_{-\mathcal{M}+1}K_l - \Gamma_l^{-1}\Phi_0) - \Phi_0, \quad (3.33)$$

where $\Gamma_l \equiv G_{\text{wg}}^{0,0}$ is the left surface Green's function, K_l and Φ_m are given by the right-propagating Bloch eigenvectors k_α^+ and the corresponding eigenstates $\phi_{m,n}^\alpha$ in the waveguides and $U_{0,1}$ is the hopping matrix between the 0-th and 1-st slices.

Chapter 4

Results

4.1 Effect of inhomogeneities on quality factors of disk microcavities (Papers I, II)

The Q -factor of a microdisk cavity is the most important parameter of the structure. It is governed by a radiative leakage through the curved interface due to diffraction. An estimation of the Q -factor in an ideal disk cavity of a typical diameter $d \sim 10\mu\text{m}$ for a typical WG resonance gives $Q \sim 10^{13}$. At the same time, reported experimentally measured values are typically in the range of $10^3 \sim 10^4$ [6] or even lower. Such the discrepancy may be attributed to different reasons like side-wall imperfections, finite or inhomogeneous height of the disk, non-uniform refractive index within the structure, effects of coupling to the substrate or pedestal and others. Several experimental observations point out side-wall imperfections as the main factor affecting the Q -value of the cavity [9; 6; 10] and can be considered of extreme importance for the design and tailoring of lasing microdisks.

Using the developed scattering-matrix method we have studied the effect of cavity roughness and inhomogeneity of the refractive index on quality factors of disk microcavities. A cavity with diameter $d = 10\mu\text{m}$ and refractive index $\langle n \rangle = 1.8$ is considered. Various studies indicate that a typical size of the side-wall imperfections can vary in the range of 5-300 nm (representing a variation of the order of $\sim 0.05\text{-}1\%$ of the cavity radius), but their exact experimental shape is unfortunately not available. We thus model the interface inhomogeneities as a superposition of random Gaussian deviations from an ideal circle of radius R with a maximal amplitude $\Delta r/2$ and a characteristic distance between the deviation maxima $\Delta l \sim 2\pi R/50$, see inset to Fig. 4.1(a). According to Fig. 3.3 the imperfect region is discretized into 100 concentric strips.

Figure 4.1(a) illustrates calculated Q -values of the disk resonant cavity for

different surface roughnesses Δr in some representative wavelength interval for TM polarization. Note that we have studied a number of different resonances and all of them showed the same trends described below.

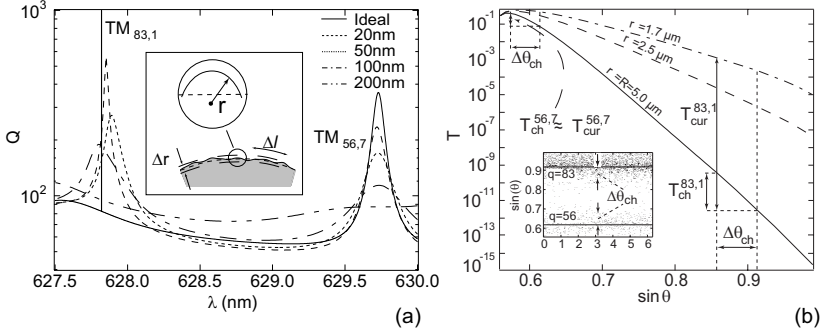


Figure 4.1: (a) Dependencies $Q = Q(\lambda)$ for two representative modes $TM_{83,1}$ (high- Q mode) and $TM_{56,7}$ (low- Q mode) for different surface roughness Δr . Inset sketches inhomogeneous surface geometry. (b) Dependence $T = T(\theta)$ for several radii of curvature ρ according to Eq. (2.3). Inset shows a Poincaré SoS for the states $q = 83$ and $q = 56$ for the cavity with $\Delta r = 0$ (straight lines of $\theta = \text{const}$) and $\Delta r = 20\text{nm}$.

The solid curve in Fig. 4.1 (a) corresponds to an ideal disk cavity without imperfections. The dependence of the averaged Q -values on the surface roughness Δr for several representative resonances is also given. A common feature of all high- Q resonances is a drastic decrease of their maximal Q -value that occurs even for very small values of $\Delta r \lesssim \lambda/20$. For example, the Q -value of resonant state $TM_{83,1}$ drops from $Q \approx 10^{13}$ for an ideal disk to $Q \approx 10^3$ for surface roughness of only $\Delta r = 20\text{nm}$. However, the picture for low- Q states is rather different. Low- Q resonances show a relatively slow decrease in their Q -values over the range of variation of Δr . For example, for the same surface roughness $\Delta r = 20$ the Q -value of resonant state $TM_{56,7}$ decreases only by a factor of 1.5, dropping from $Q \approx 300$ to $Q \approx 200$.

In order to understand this behavior we combine a *Poincaré surface of section (SoS)* method with analysis of ray reflection at a curved dielectric interface (see Eq. (2.3)). Figure 4.1(b) illustrates that transmission T , calculated by Eq. (2.3), decreases exponentially as the difference between angle of incidence θ and critical angle of incidence θ_c grows. Poincaré SoS represents dependence of angle of incidence θ on the polar angle φ around the cavity, its detailed definition and related discussion are given in Paper II. The inset to Fig. 4.1(b) depicts the SoS for two states with $q = 56$ and 83 shown in Fig. 4.1(a), where the initial angle of incidence θ_0 of launched rays is related to the angular number

q . The SoS demonstrates that initially regular dynamics of an ideal cavity (straight line) transforms into a chaotic one even for a cavity with maximum roughness $\Delta r \lesssim 20\text{nm}$. $\Delta T_{\text{ch}}^{83,1}$ in Fig. 4.1(b) indicates the estimated increase in the transmission coefficient due to the broadening of the phase space, $\Delta\theta_{\text{ch}}$, as extracted from the Poincaré SoS for the state with $q = 83$. This corresponds to the decrease of $\Delta Q \sim \Delta T^{-1} \approx 10^{-2}$. This value is much smaller than the actual calculated decrease of the Q -factor for the high- Q resonance $\text{TM}_{83,1}$.

In order to explain the rapid degradation of high- Q resonances, we focus on another aspect of the wave dynamics. The imperfections at the surface boundary introduce a *local radius of surface curvature* ρ that is smaller than the disk radius R (see inset in Fig. 4.1(a)). One may thus expect that, with the presence of a local surface curvature, the total transmission coefficient will be determined by the averaged value of ρ rather than by the disk radius R . Figure 4.1(b) outlines that the reduction of the local radius of curvature from $5\mu\text{m}$ (ideal disk) to $1.7\mu\text{m}$ ($\Delta r = 20\text{nm}$) causes an increase of the transmission coefficient by $\Delta T_{\text{cur}} \approx 10^8$. This number, combined with the estimate based on the change of $\Delta T_{\text{ch}} \sim 10^2$, is fully consistent with the Q -factor decrease shown in Fig. 4.1(a). We thus conclude that *the main mechanism responsible for the rapid degradation of high- Q resonances in non-ideal cavities is the enhanced radiative decay through the curved surface* because the effective local radius (given by the surface roughness) is smaller than the disk radius R .

In contrast, for the case of low- Q resonances the change in the transmission coefficient due to enhanced radiative decay ΔT_{cur} is of the same magnitude as the change ΔT_{ch} due to the broadening of the phase space caused by the transition to chaotic dynamics (for the resonance $\text{TM}_{56,7}$ in Fig. 4.1). Therefore, both these factors play comparable roles in degradation of the low- Q WG resonances.

We have also studied the effect of the non-uniform refractive index within the cavity and found that decay of the Q -factor in that case is of minor importance in comparison to the case of rough surface.

4.2 Quantum corrals (Paper III)

We have adapted the scattering matrix technique developed for disk dielectric microcavities to study of quantum-mechanical scattering in quantum corrals, which can be considered as a nanoscale analogue to dielectric cavities. Quantum corrals consist of adatoms of noble metals or Fe, deposited by AFM on (111) surface of Cu in ring, triangle or other arrangements (see Fig. 4.2). Cu surface states interact strongly with adatoms, and the spatial variation of the STM differential conductance reveals beautiful images of the surface standing wave patterns in the quantum corrals. In addition, the experiments show a series of remarkable resonant peaks in the energy spectrum of the differential

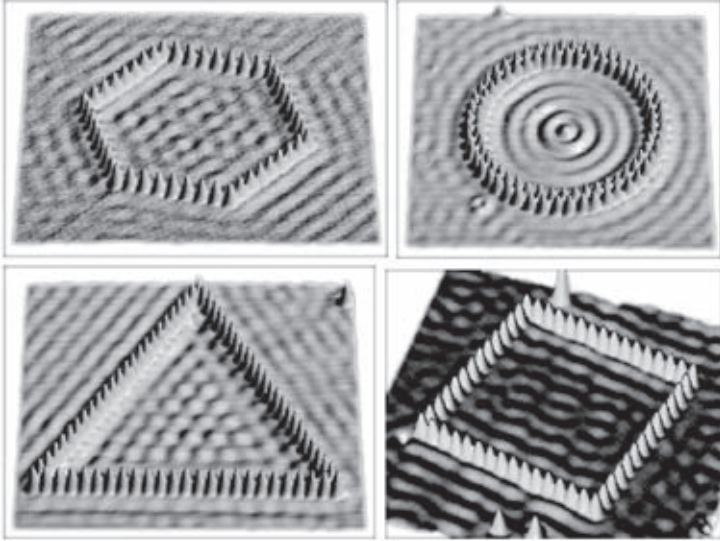


Figure 4.2: Quantum corral structures. STM images, reported by IBM [51]

conductance dI/dV at the center of the structures. So far there were several reports on experimental and theoretical studies of the corral structures. In order to describe the experimental observation [47; 48], Heller *et al.* [52] have developed the multiple-scattering theory for surface electron waves in quantum corrals. In that theory each adatom was treated as a point-like "black dot" δ -function potential supporting isotropic scattering of a standing wave. The quantitative agreement with the experiment was achieved by considering an additional inelastic channel of scattering to the bulk of the substrate. It was also concluded that absorption is the dominant mechanism for the broadening of the energy levels seen in the experiment. Their theory describes well the spatial distribution of the wave function in the corrals, but overestimates the broadening of the resonant peaks, especially at higher energies.

An alternative purely elastic scattering theory for the same quantum corral structures was drawn by Harbury and Porod [53]. They described the adatoms by finite-height solid potential barriers. Their findings suggest that the features of the spectrum and the wavefunction distribution can be extremely sensitive to the detailed shape of the scattering potential.

The advance of our scattering matrix method is that *it can treat a realistic potential of the adatoms, their displacements or variety of inhomogeneities*. Accounting for a realistic smooth shape of a scattering potential is known as crucial for quantitative description of many phenomena in quan-

tum nanostructures. The potential of each adatom is taken as a Gaussian with the half-width σ and the height V_0 centered at the location (x_0, y_0) , $V(x, y) = V_0 \exp[-(x - x_0)^2/2\sigma^2] \exp[-(y - y_0)^2/2\sigma^2]$.

Using the scattering matrix technique we calculate the bias voltage dependence and the spatial distribution of the local density of states (LDOS) for 60-Fe-adatom, 88.7-Å-radius circular quantum corrals reported by Heller *et al.* [52]. Fig. 4.3 shows experimental and theoretical results for voltage dependence (a) and the spatial distribution (b) of the LDOS. The Fe-adatoms are located on the meshes of a 2.55Å triangular grid corresponding to the hexagonal Cu(111) lattice. The effective mass used in all the simulations is taken $m^* = 0.361m_0$ and the electron band-edge energy $E_0 = 0.43\text{eV}$ below the Fermi energy of the electrons.

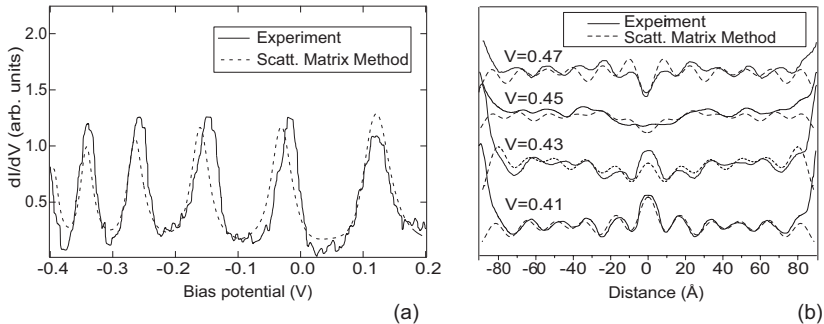


Figure 4.3: (a) The experimental spectrum of the differential conductance dI/dV at the center of the 88.7-Å-radius 60-Fe-adatom circular quantum corral structure on Cu(111) substrate (solid curve). Scattering matrix technique applied for a smooth adatom potential with height $V_0 = 2.5\text{eV}$ and broadening $\sigma = 1.52\text{Å}$ (dashed line). (b) The experimental curves (solid lines) and results of scattering-matrix simulations (dashed line) for the local density of states subject to the tip position inside a circular corral for low bias voltages.

Our calculations prove the importance of the accounting for a realistic potential and reproduce quantitatively all the experimental observations (see Paper III for the details), which is in contrast to previous theories (treating the adatoms as point scatterers) that require additional inelastic channels of scattering into the bulk in order to achieve the agreement with the experiment. Our findings thus indicate that surface states are not coupled to the bulk electrons.

4.3 Surface-state lasers (Paper IV)

As it has been already mentioned in Chapter 2, surface states in photonic crystals can be exploited in variety of lasing, sensing and waveguiding applications. First we focus on the novel type of lasing cavity that is situated on the surface of a photonic crystal and uses surface modes.

For this purpose we apply the developed Green's function technique. We consider a semi-infinite square-lattice photonic crystal composed of cylinders with $\varepsilon = 8.9$ and diameter $D = 0.4a$ (a is a lattice constant) in air background. In order to create surface geometry sustaining surface modes, we reduce the diameter of rods in the outmost row to $d = 0.2a$. This structure has the full fundamental bandgap for TM-polarization in the range $0.33 < \omega a/2\pi c < 0.44$ and supports one surface mode, which along with band structure is depicted in Fig. 2.9(a). In order to create a surface-state lasing cavity the modified surface region has to be confined along the modified boundary that turns the surface mode into a resonant state with a finite lifetime. For this sake a semi-infinite photonic crystal structure containing only a finite number N of the surface rods of the reduced diameter $d = 0.2a$ was considered. These rods define a *resonant cavity* situated at the surface of the photonic crystal as illustrated in the inset to Fig. 4.4(a) for the case of $N = 6$. The strong confinement from three sides of the cavity is provided by the photonic crystal operating in the bandgap.

In order to calculate the quality factor of the structure at hand, we illuminate the surface resonant cavity semi-infinite photonic crystal by an incidence wave, which excites the resonant mode within the cavity, compute the intensity of the field distribution and express Q -factor as $Q = \omega\Omega/(4 \int S_{in} dy)$ [50], where Ω characterizes the energy stored in the system and the integral over S_{in} is the incoming energy flux. It should be stressed that the value of the Q -factor at resonance depends on the coupling of the surface state modes with the *outgoing* radiation, and thus is independent of the incidence angle of the incoming wave.

Figure 4.4(a) shows the calculated Q -factor of the resonant cavity versus the frequency of the illuminating light. In the given frequency interval there are three lasing peaks with quality factors $\sim 10^5$. Note that above values might underestimate the actual theoretical Q -factors obtained within present 2D calculations, because even finer frequency steps in the vicinity of the resonances are required for better resolution of the Q -factors. The estimation of the position of the peaks for the cavity at hand can be performed making use a formula for Fabry-Perot resonator, whose resonant wavelengths are given by $\lambda_\alpha = 2\pi/k_\alpha$, with the wavevector $k_\alpha = \pi\alpha/w$. From dispersion relation (upper panel of 4.4(a)) it follows that only modes $\alpha = 5, 6, 7$ are situated inside the frequency interval where the surface mode exists. An estimation of the expected positions for the resonant peaks for these modes is also given in the lower panel of Fig. 4.4(a) where the discrepancy between the expected

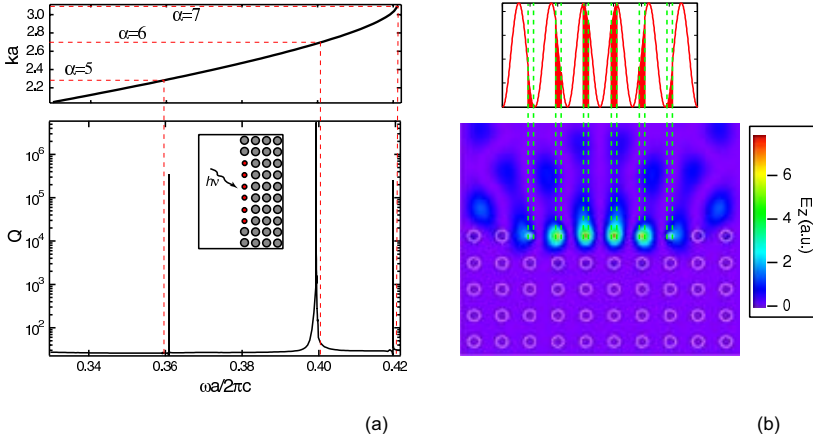


Figure 4.4: (a) Lower panel: Spectrum of a surface state photonic bandgap cavity. Inset illustrates the resonant cavity defined by the $N = 6$ surface rods of the smaller diameter $d = 0.2a$ placed on the photonic crystal surface. Upper panel: The dispersion relation for the surface state for the semi-infinite photonic crystal. The dashed lines indicate the expected analytical resonant wave vectors for the modes $\alpha = 5, 6, 7$ and corresponding expected resonant frequencies. (b) Lower panel: Calculated intensity of the E_z component for the 6-th mode shown in Fig. 4.4(a). Upper panel: Expected field intensity at different rods is given by the overlap of the 6th eigenstate of the cavity with the actual positions of the rods.

analytical and calculated resonance frequencies does not exceed 0.5%.

Figure 4.4(b) depicts the intensity of the E_z component of the electromagnetic field for the resonance mode $\alpha = 6$. As expected for TM-modes, the field is localized in the cavity inside the rods, and the intensity decays very rapidly both to the open space and to the photonic crystal. The field intensity at different rods in the cavity is expected to be determined by the overlap of the α th eigenstate of the Fabry-Perot resonator with the actual positions of the rods in the cavity. This overlap for the 6th mode is also shown in Fig. 4.4(b), which agrees perfectly with the actual calculated field intensity.

4.4 Surface-state waveguides (Paper V)

”Conventional” waveguides in photonic crystals represent line defects in periodic structures supporting guided Bloch modes whose frequency region lies in the bandgap. These modes are strongly confined within the waveguide region

and can propagate lossless to substantial distances. Here we propose a novel type of waveguiding structures, namely waveguides that operate on surface modes of semi-infinite photonic crystals (surface modes, propagating along the boundary are now waveguiding modes!) and *are located on the surface of a PC*. Their "non-traditional" location may open up new possibilities for design and operation of photonic structures for feeding and redistributing light in PCs.

Making use the Green's function technique we have studied localization properties of surface modes, their dispersion relations and effect of inhomogeneities. The latter has been demonstrated as the one having the strongest impact on the performance of lasing microcavities. One can expect then, that imperfections in a shape of the rods, their displacement, or variation of the refraction index throughout the crystal may also cause a strong negative effect on the waveguiding efficiency of the surface modes.

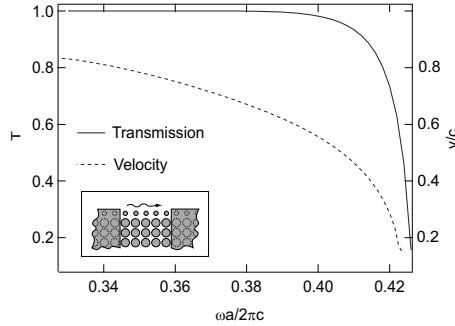


Figure 4.5: Transmission coefficient (solid line, left axis) for surface modes propagating in a non-ideal surface-mode waveguide. Velocity of the surface mode (dashed line, right axis) from Fig. 2.9. Inset shows the structure under study, where the shaded regions denote ideal semi-infinite waveguides, and the central region of the width of $5a$ represents an imperfect photonic crystal where scattering of the Bloch surface state takes place.

We consider the same semi-infinite photonic crystal as in the previous Section ($\varepsilon = 8.9$, $D = 0.4a$) with the infinitely long boundary consisting of rods of reduced diameter $d = 0.2a$ (see band structure in Fig. 2.9). In order to study the effect of imperfections, the structure is split into three regions as shown in the inset to Fig. 4.5. Two of them are left and right semi-infinite periodic structures (perfect waveguides for surface modes), and the block of the PC in between is an imperfect region. Utilization of the Green's function technique allows one to use surface Bloch modes as scattering states that propagate in perfect waveguides from the infinity into the imperfect region where they undergo scattering. Obviously, in the case when the scattering region is absent

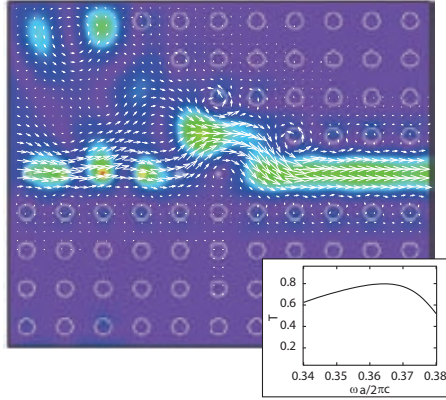


Figure 4.6: A lead-in coupler composed of a surface-state waveguide to the left and a conventional tapered PC waveguide to the right. The size of the surface rods gradually decreases to zero in the central region where the surface-state waveguide transforms in a conventional PC waveguide. Intensity distribution is shown for E_z -component of the electromagnetic field at $\omega a / 2\pi c \approx 0.365$. Arrows sketch the flow of the Poynting vector. Inset shows transmission coefficient subject to the energy of incoming light. Parameters of the photonic crystal correspond those in Section 4.3.

(perfect waveguides are attached to each other), the Bloch states propagate freely without any losses. The imperfection is modelled by the discretization of the scattering region different from that in the left and right perfect waveguides.

The transmission coefficient in Fig. 4.5 for the surface mode drops quite rapidly in the energy regions corresponding to the low velocity of the surface state (dashed line in the Figure). This is because the backscattering probability is greatly enhanced for the low-speed states. Even for 5 imperfect unit cells the transmission coefficient in energy region $\omega a / 2\pi c \gtrsim 0.40$ is less than 1 which makes this energy region hardly appropriate for waveguiding purposes. For lower energies the structure seems a good candidate for a waveguide.

In order to illustrate the possible applications of surface-state waveguides two novel devices have been proposed. The first one is light coupler that enables feeding external light into photonic-crystal waveguides. Fig. 4.6 illustrates the proposed structure.

In this device the external light first couples to surface-state region, then the surface mode enters a tapered region, where it adiabatically (the diameter of the surface rods in the surface-state waveguide gradually decreases to zero) is transformed into conventional waveguiding state. The maximum achieved transmission reaches $T \approx 0.8$ (see inset to Fig. 4.6), which is even higher

than the transmission in conventional tapered [54] or mode-matched structures [55; 56].

The second device proposed is a directional emitter. We demonstrate, that directional emission with the angular spread much less than in conventional waveguides can also be achieved for the case of surface-state waveguides coupled to air. Figure 4.7 shows E_z field intensity (a) and the directional diagram (b) for the surface state propagating in a semi-infinite waveguide.

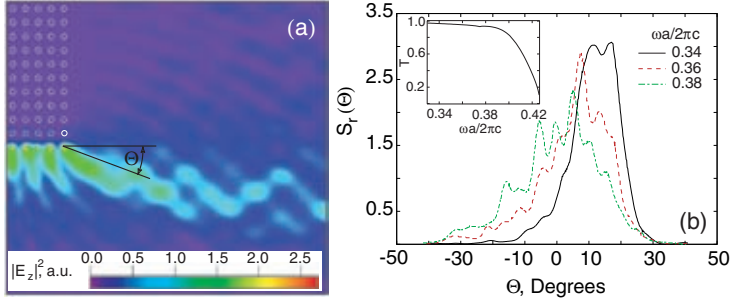


Figure 4.7: (a) Intensity distribution for E_z -component of the electromagnetic field in the surface-mode waveguide terminated to air for $\omega a/2\pi c = 0.34$. (b) Far-field radial component of the Poynting vector $S_r(\Theta)$ radiated out of a surface-mode waveguide versus azimuthal angle Θ for different $\omega a/2\pi c$. Inset shows the transmission coefficient for the surface state as a function of the frequency.

The most of the beam intensity is localized within a cone $\Delta\Theta \sim 20^\circ$. Such the narrow beaming originates from the fact that the surface state is localized in a wide spatial region near the surface $\lesssim 10a$ (see discussion on localization in Paper V), as opposed to conventional waveguides, whose width is typically $\sim a$ and the corresponding diffraction cone is about 70° . The angular spread in this case due to the diffraction, $\sin \Theta \sim \frac{\lambda}{10a}$, is consistent with the calculated far-field radial distribution of the Poynting vector. As the frequency of the incoming light increases, the surface mode becomes more localized, and the spread of the outgoing radiation increases. The effect of directional beaming in surface-mode waveguides might find its practical application for integration of PC-based devices with conventional fiber-optics.

Bibliography

- [1] K. J. Vahala. Optical microcavities. *Nature*, 424:839–846, Aug. 2003.
- [2] A. V. Snyder and J. D. Love. Reflection at a curved dielectric interface – electromagnetic tunneling. *IEEE Trans. Microwave. Theor. Techn.*, MTT-23:134–141, 1975.
- [3] F. T. Smith. Lifetime matrix in collision theory. *Phys. Rev.*, 118, 1960.
- [4] R. C. Polson, Z. Vardeny, and D. A. Chinn. Multiple resonances in microdisk lasers of π -conjugated polymers. *Appl. Phys. Lett.*, 81:1561–1563, 2002.
- [5] D. K. Armani, T. J. Klippenberg, S. M. Spillane, and K. J. Vahala. Ultra-high- Q toroid microcavity on a chip. *Lett. to Nature*, 421:925–928, Feb. 2003.
- [6] B. Gayral, J. M. Gérard, A. Lemaitre, C. Dupuis, L. Manin, and J. L. Pelouard. High- Q wet-etched GaAs microdisks containing InAs quantum boxes. *Appl. Phys. Lett.*, 75(13):1908–1910, Sep. 1999.
- [7] D. W. Vernooy, V. S. Ilchenko, H. Mabuchi, E. W. Streed, and H. J. Kimble. High- Q measurements of fused-silica microspheres in the near infrared. *Opt. Lett.*, 23:247–249, 1998.
- [8] M. Kutawa-Gonokami and K. Takeda. Polymer whispering gallery mode lasers. *Opt. Mater.*, 9:12–17, 1998.
- [9] M. Fujita, K. Inoshita, and T. Bata. Room temperature continuous wave lasing characteristics of GaInAs/InP microdisk injection laser. *Electronic Lett.*, 34:278–279, 1998.
- [10] C. Seassal, X. Letartre, J. Brault, M. Gendry, P. Pottier, P. Viktorovitch, O. Piquet, P. Blondy, D. Cros, and O. Marty. InAs quantum wires in InP-based microdiscs: Mode identification and continuous wave room temperature laser operation. *J. Appl. Phys.*, 88:6170–6174, 2000.

- [11] <http://ab-initio.mit.edu/photons/index.html>.
- [12] Z. Zhang and M. Qiu. Small-volume waveguide-section high- Q microcavities in 2D photonic crystal slabs. *Opt. Express*, 12(17):3988–3995, Aug. 2004.
- [13] M. Notomi, A. Shinya, S. Mitsugi, E. Kuramochi, and H.-Y. Ryu. Waveguides, resonators and their coupled elements in photonic crystal slabs. *Opt. Express*, 12(8):1551–1561, Apr. 2004.
- [14] S.-H. Kwon, H.-Y. Ryu, G.-H. Kim, Y.-H. Lee, and S.-B. Kim. Photonic bandedge lasers in two-dimensional square-lattice photonic crystal slabs. *Appl. Phys. Lett.*, 89(19):3870–3872, Nov. 2003.
- [15] J.-K. Yang, S.-H. Kim, G.-H. Kim, H.-G. Park, Y.-H. Lee, and S.-B. Kim. Slab-edge modes in two-dimensional photonic crystals. *Appl. Phys. Lett.*, 84:3016–3018, Apr. 2004.
- [16] S. Xiao and M. Qiu. Surface mode microcavities. *Appl. Phys. Lett.*, 87(11):111102, 2005.
- [17] S. Fan, S. G. Johnson, J. D. Joannopoulos, C. Manolatou, and H. A. Haus. Waveguide branches in photonic crystals. *J. Opt. Soc. Am. B*, 18:162–165, Feb. 2001.
- [18] S. Fan, P. R. Villeneuve, and J. D. Joannopoulos. Channel drop tunneling through localized states. *Phys. Rev. Lett.*, 80:960–963, Feb. 1998.
- [19] J. S. Foresi, P. R. Villeneuve, J. Ferrera, E. R. Thoen, G. Steinmeyer, S. Fan, J. D. Joannopoulos, L. C. Kimerling, Henry I. Smith, and E. P. Ippen. Photonic-bandgap microcavities in optical waveguides. *Lett. to Nature*, 390:143–145, Nov. 1997.
- [20] M. F. Yanik, S. Fan, M. Soljačić, and J. D. Joannopoulos. All-optical transistor action with bistable switching in a photonic crystal cross-waveguide geometry. *Opt. Lett.*, 28(24):2506–2508, Dec. 2003.
- [21] J. D. Joannopoulos, R. D. Meade, and J. N. Winn. *Photonic crystals: Molding the Flow of Light*. Princeton University Press, Princeton, 1995.
- [22] F. Ramos-Mendieta and P. Halevi. Surface electromagnetic waves in two-dimensional photonic crystals: Effect of the position of the surface plane. *Phys. Rev. B*, 59:15112–15120, Jun. 1999.
- [23] X. Zhang and L.-M. Li, Z.-Q. Zhang, and C. T. Chan. Surface states in two-dimensional metallodielectric photonic crystals studied by a multiple-scattering method. *Phys. Rev. B*, 63:125114, Mar. 2001.

- [24] J. M. Elson and K. Halterman. Local density of states analysis of surface wave modes on truncated photonic crystal surfaces with nonlinear material. *Opt. Express*, 12:4855–4863, Oct. 2004.
- [25] E. Moreno, F. J. García-Vidal, and L. Matrín-Moreno. Enhanced transmission and beaming of light via photonic crystal surface modes. *Phys. Rev. B*, 69:121402(R), Mar. 2004.
- [26] K. S. Yee. Numerical solution of initial boundary-value problems involving maxwell’s equations in isotropic media. *IEEE Trans. Ant. Prop.*, AP-14:302–307, 1966.
- [27] J.-P. Berenger. A perfectly matched layer for the absorption of electromagnetic waves. *J. Comput. Phys.*, 114(2):185–200, Oct. 1994.
- [28] A. Mekis, J. C. Chen, I. Kurland, S. Fan, P. R. Villeneuve, and J. D. Joannopoulos. High transmission through sharp bends in photonic crystal waveguides. *Phys. Rev. Lett.*, 77:3787–3790, Oct. 1996.
- [29] P. C. Waterman. Symmetry, unitarity and geometry in electromagnetic scattering. *Phys. Rev. D*, 3:825–839, 1971.
- [30] M. I. Mishchenko, L. D. Travis, and A. A. Lacis. *Scattering, Absorption, and Emission of Light by Small Particles*. Cambridge University Press, Cambridge, 2002.
- [31] P. A. Knipp and T. L. Reinecke. Boundary-element method for the calculation of the electronic states in semiconductor nanostructures. *Phys. Rev. B*, 54:1880–1891, 1996.
- [32] J. Wiersig. Boundary element method for resonances in dielectric micr-cavities. *J. Opt. A: Pure Appl. Opt.*, 5:53–60, 2003.
- [33] S. V. Boriskina, T. M. Benson, P. Sewell, and A. I. Nosich. Highly efficient design of spectrally engineered whispering-gallery-mode microlaser resonators. *Opt. and Quant. Electr.*, 35:545–559, 2003.
- [34] K. M. Ho, C. T. Chan, and C. M. Soukoulis. Existence of a photonic gap in periodic dielectric structures. *Phys. Rev. Lett.*, 65(25):3152–3155, Dec. 1990.
- [35] D. Cassagne, C. Jouanin, and D. Bertho. Hexagonal photonic-band-gap structures. *Phys. Rev. B*, 53(11):7134–7142, Mar. 1996.
- [36] Z.-Y. Li, J. Wang, and B.-Y. Gu. Creation of partial band gaps in anisotropic photonic-band-gap structures. *Phys. Rev. B*, 58(7):3721–3729, Aug. 1998.

- [37] S. Shi, C. Chen, and D. W. Prather. Revised plane wave method for dispersive material and its application to band structure calculations of photonic crystal slabs. *Appl. Phys. Lett.*, 86:043104 1–3, Jan. 2005.
- [38] J. B. Pendry. Calculating photonic band structure. *J. Phys.: Condens. Matter*, 8:1085–1108, 1996.
- [39] D. Felbacq, G. Tayeb, and D. Maystre. Scattering by a random set of parallel cylinders. *J. Opt. Soc. Am. A*, 11:2526–2538, 1994.
- [40] D. M. Whittaker and I. S. Culshaw. Scattering-matrix treatment of patterned multilayer photonic structures. *Phys. Rev. B*, 60(4):2610–2618, Jul. 1999.
- [41] Z.-Y. Li and K.-M. Ho. Light propagation through photonic crystal waveguide bends by eigenmode examinations. *Phys. Rev. B*, 68:045201 1–12, Jul. 2003.
- [42] Z.-Y. Li and K.-M. Ho. Light propagation in semi-infinite photonic crystals and related waveguide structures. *Phys. Rev. B*, 68:155101 1–15, Oct. 2003.
- [43] E. Moreno, D. Erni, and C. Hafner. Modeling of discontinuities in photonic crystal waveguides with the multiple multipole method. *Phys. Rev. E*, 66:036618 1–12, Sep. 2002.
- [44] O. J. F. Martin, C. Girard, and A. Dereux. Generalized field propagator for electromagnetic scattering and light confinement. *Phys. Rev. Lett.*, 74(4):526–529, Jan. 1995.
- [45] V. V. Nikolsky and T. I. Nikolskaya. *Decomposition approach to the problems of electrodynamics*. Nauka, Moskow, 1983. in Russian.
- [46] S. Datta. *Electronic Transport in Mesoscopic Systems*. Cambridge University Press, Cambridge, 1995.
- [47] M. F. Crommie, C. P. Lutz, , and D. M. Eigler. Imaging standing waves in a two-dimensional electron gas. *Nature*, 363:524–527, Jun. 1993.
- [48] M. F. Crommie, C. P. Lutz, and D. M. Eigler. Confinement of electrons to quantum corrals on a metal surface. *Science*, 262:218–220, Oct. 1993.
- [49] D. K. Ferry and S. M. Goodnik. *Transport in Nanostructures*. Cambridge University Press, Cambridge, 1997.
- [50] K. Sakoda. *Optical properties of photonic crystals*. Springer, Berlin, 2001.
- [51] <http://www.almaden.ibm.com/vis/stm/corral.html>.

- [52] E. J. Heller, M. F. Crommie, C. P. Lutz, and D. M. Eigler. Scattering and absorption of surface electron waves in quantum corrals. *Lett. to Nature*, 369:464–466, Jun. 1994.
- [53] H. K. Harbury and W. Porod. Elastic scattering theory for electronic waves in quantum corrals. *Phys. Rev. B*, 53:15455-15458, Jun. 1996.
- [54] A. Mekis and J. D. Joannopoulos. Tapered couplers for efficient interfacing between dielectric and photonic crystal waveguides. *IEEE J. Lightwave Technol.*, 19:861–865, Jun. 2001.
- [55] P. Sanches, P. Bienstman, B. Luyssaert, R. Baets, and J. Marti. Analysis of butt coupling in photonic crystals. *IEEE J. Quant. Electron.*, 40:541–550, May 2004.
- [56] R. Stoffer, H. Hoekstra, R. M. De Ridder, E. V. Groesen, , and F. P. H. Van Beckum. Numerical studies of 2D photonic crystals: Waveguides, coupling between waveguides and filters. *Opt. Quant. Electron.*, 32:947–961, Aug. 2000.